

Magnetic reconnection resulting from flux emergence: implications for jet formation in the lower solar atmosphere?

J. Y. Ding^{1,2}, M. S. Madjarska¹, J. G. Doyle¹, Q. M. Lu², K. Vanninathan¹, and Z. Huang¹

¹ Armagh Observatory, College Hill, Armagh BT61 9DG, N. Ireland
e-mail: jyd@arm.ac.uk

² School of Earth and Space Sciences, University of Science and Technology of China, Hefei 230026, PR China

Received 17 June 2011 / Accepted 26 September 2011

ABSTRACT

Aims. We aim at investigating the formation of jet-like features in the lower solar atmosphere, e.g. chromosphere and transition region, as a result of magnetic reconnection.

Methods. Magnetic reconnection as occurring at chromospheric and transition regions densities and triggered by magnetic flux emergence is studied using a 2.5D MHD code. The initial atmosphere is static and isothermal, with a temperature of 2×10^4 K. The initial magnetic field is uniform and vertical. Two physical environments with different magnetic field strength (25 G and 50 G) are presented. In each case, two sub-cases are discussed, where the environments have different initial mass density.

Results. In the case where we have a weaker magnetic field (25 G) and higher plasma density ($N_e = 2 \times 10^{11} \text{ cm}^{-3}$), valid for the typical quiet Sun chromosphere, a plasma jet would be observed with a temperature of $2-3 \times 10^4$ K and a velocity as high as 40 km s^{-1} . The opposite case of a medium with a lower electron density ($N_e = 2 \times 10^{10} \text{ cm}^{-3}$), i.e. more typical for the transition region, and a stronger magnetic field of 50 G, up-flows with line-of-sight velocities as high as $\sim 90 \text{ km s}^{-1}$ and temperatures of 6×10^5 K, i.e. upper transition region – low coronal temperatures, are produced. Only in the latter case, the low corona Fe IX 171 Å shows a response in the jet which is comparable to the O V increase.

Conclusions. The results show that magnetic reconnection can be an efficient mechanism to drive plasma outflows in the chromosphere and transition region. The model can reproduce characteristics, such as temperature and velocity for a range of jet features like a fibril, a spicule, a hot X-ray jet or a transition region jet by changing either the magnetic field strength or the electron density, i.e. where in the atmosphere the reconnection occurs.

Key words. Sun: corona – Sun: transition region – Sun: chromosphere – Sun: magnetic topology

1. Introduction

A variety of jet-like features such as spicules, fibrils, surges, Ellerman bombs, EUV/X-ray jets etc., as seen in various atmospheric regions, are observed in the solar atmosphere. Spicules are relatively thin, elongated jet-like structures best viewed at the solar limb in H α or Ca II images as bright features against a dark background. The close correlation between observed properties of limb spicules and other on-disk features such as mottles, fibrils and straws has prompted many authors to suggest that these may be counterparts of each other (Tsiropoula & Schmieder 1997). As viewed in the optical, the classical spicule is observed to reach heights of 6500–15 000 km (Beckers 1968; Withbroe 1983) with an average lifetime of 5 min and average plasma velocities of 25 km s^{-1} . Recently, using high-resolution observations in Ca II H (3968 Å) from the Solar Optical Telescope (SOT) on Hinode, De Pontieu et al. (2007) suggested at least two types of spicules, the classical spicule and a more dynamic one.

Tavabi et al. (2011) suggested four types of spicules based on their diameter, ranging from $0.3''$ (220 km), $0.5''$ (360 km), $0.75''$ (550 km) to $1.15''$ (850 km). Typically, they show a succession of upward and downward motions. The more dynamic spicule develop and disappear on timescales of 10–60 s, with velocities sometimes exceeding 100 km s^{-1} .

Spicules are also seen in UV and EUV lines (Dere et al. 1989) and thus reach at least to transition region temperatures.

Cook et al. (1984) using HRTS observations taken in C IV 1550 Å showed that these structures show tilted features which was interpreted as rotational velocities of approximately 50 km s^{-1} . In a more recent paper, Madjarska et al. (2011a) showed that this may be better interpreted as a multi-strand structure with up-flows and down-flows.

Several authors have looked at magnetic reconnection as a driving mechanism for hot jets (Jin et al. 1996; Innes & Tóth 1999; Galsgaard et al. 2005; Nishizuka et al. 2008; Patsourakos et al. 2008; Murray et al. 2009; Rosdahl & Galsgaard 2010; Pariat et al. 2010, and references therein). Roussev et al. (2001a,b,c) performed 2D Magneto-hydrodynamic (MHD) simulations of transition region jets deriving blue-shifts of the order of 100 km s^{-1} . Several initial physical environments were studied. However, the plasma β on the current sheet was the same in all the cases with the maximum velocity of the blue-shifted jets eventually reaching almost the same value in all cases, although they were different at the beginning of the experiments.

Various authors have suggested that spicules can be driven by waves (magnetoacoustic or Alfvén) (Hansteen et al. 2006; De Pontieu et al. 2007; Heggland et al. 2007), while Sterling et al. (1993), Karpen et al. (1995), and Heggland et al. (2009) have considered magnetic reconnection as a plausible candidate for driving chromospheric jets. In all the models mentioned above, spicules are produced but their velocities are small ($\sim 25 \text{ km s}^{-1}$). Martínez-Sykora et al. (2011b) explored 3D

simulations of flux emergence, and reported on more dynamic features that reached coronal temperatures. In their model, large tangential discontinuities of magnetic field is necessary to create the conditions for accelerating the jets. These large magnetic field gradients lead to strong Lorentz forces, causing horizontal flows which reach a “wall” of strong vertical magnetic field. The wall squeezes the plasma and forces a large increase in the pressure, deflecting the horizontal flows and pushing them to move vertically.

Pariat et al. (2009) proposed a 3D model for solar polar jets, where the magnetic twist was taken as the jet driver. The release of magnetic twist onto open field lines by magnetic reconnection resulted in high-speed jets. Their work reproduced helical structures observed in some polar-hole jets (Patsourakos et al. 2008). Jiang et al. (2011) examined the influence of different initial reconnection angles by using a 3D MHD model where thermal conduction and gravity were neglected. Fan-shaped jets moving along the magnetic guide field were obtained.

Recently, Ding et al. (2010) used a 2.5-dimensional resistive MHD model in Cartesian coordinates to investigate magnetic reconnection in the low atmosphere, e.g. chromosphere, discussing the implications for jet features at transition-region temperatures. They showed that faster and hotter outflows could be obtained if a physical environment with lower mass density was considered, however, the highest temperature of the plasma heated by magnetic reconnection is only 5×10^5 K in their study.

Here, we expand the work of Ding et al. (2010) varying the electron density and field strength as applied to a larger range of jet features, including fibrils, spicules, chromospheric jets and transition region jets. This work uses a larger grid model (see later) than the previous study. Here, we also look at jet formations as viewed in different parts of the lower solar atmosphere. We derive the response of three spectral lines with formation temperatures from the lower transition region to the low corona, as obtained in the foot-points and in the jet itself. The 2.5-D resistive MHD model is briefly described in Sect. 2. Section 3 gives the numerical results and the derived line profiles. Conclusions and discussion are drawn in Sect. 4.

2. Physical model and numerical methods

2.1. Basic equations

A 2.5-dimensional resistive MHD model in Cartesian coordinates is used here. The MHD equations are the same as presented in Ding et al. (2010), where ρ , v , ψ , B_z , T , p , j , \mathbf{B} , \mathbf{g} , η , γ , β_0 , Q , L_r are the mass density, flow velocity, magnetic flux function, z -component of magnetic field, temperature, gas pressure, electric current density, magnetic field, gravitational acceleration, dimensionless magnetic diffusivity, adiabatic index, characteristic ratio of the gas pressure to the magnetic pressure deduced from the basic units, heat conduction, and radiative losses, respectively. And, p , j , \mathbf{B} , Q , L_r are explicitly expressed by

$$p = \rho T, \quad j = \nabla \times \mathbf{B}, \quad \text{and} \quad \mathbf{B} = \nabla \times (\psi \hat{z}) + B_z \hat{z}, \quad (1)$$

$$Q = \nabla \cdot [T^{5/2}(\mathbf{B} \cdot \nabla T)\mathbf{B}/B^2], \quad \text{and} \quad L_r = \rho^2 \Lambda(T), \quad (2)$$

where $\Lambda(T)$ is the radiative loss function. Here, optical depth effects are considered: at $T \leq 2 \times 10^4$ K, $\Lambda(T)$ is reduced to zero; At $2 \times 10^4 < T < 10^5$ K, $\Lambda(T)$ suggested by McClymont & Canfield (1983) is used; At $T \geq 10^5$ K, $\Lambda(T)$ calculated by Cook et al. (1989) is adopted. The characteristic values taken as basic units for the mass density, temperature, length, and magnetic field strength are: $\rho_0 = 3.34 \times 10^{-10}$ kg m $^{-3}$, corresponding to

Table 1. Parameters of the four initial states, namely A1, A2, B1, and B2, including the characteristic values of the Alfvén velocity (v_A) and plasma β in each state.

ρ_{b0}	ψ_{b0}	2	1
1	A1	$v_A = 244$ km s $^{-1}$	$v_A = 122$ km s $^{-1}$
		$\beta = 1.1 \times 10^{-2}$	$\beta = 4.4 \times 10^{-2}$
0.1	A2	$v_A = 772$ km s $^{-1}$	$v_A = 386$ km s $^{-1}$
		$\beta = 1.1 \times 10^{-3}$	$\beta = 4.4 \times 10^{-3}$

the electron number density $N_e = 2 \times 10^{11}$ cm $^{-3}$, $T_0 = 10^4$ K, $L_0 = 500$ km, and $B_0 = 25$ G, respectively. The dimensionless coefficients of the heat conduction and radiative losses are in the same forms as given by Ding et al. (2010).

The dimensionless size of the computational domain is $0 \leq x \leq 6$ and $0 \leq y \leq 6$, divided into 500×500 grid points (in the Ding et al. 2010, work a smaller grid of 400×400 was adopted). Uniform meshes are adopted in both x - and y -directions. In the present study, x is the horizontal axis, and y is vertical, representing the height of the solar atmosphere. At the bottom, all quantities are fixed. Other boundaries are treated as open, and all quantities are calculated in terms of equivalent extrapolation. A multi-step implicit scheme (Hu 1989) is used to solve the MHD equations.

2.2. Initial state

The initial magnetic field is a potential one taken to be in the following form

$$\begin{cases} \psi = -\psi_{b0}x, \\ B_z = 0, \end{cases} \quad (3)$$

where ψ_{b0} is a free parameter used to control the magnetic field strength of the initial background. The initial magnetic field is different from that used in Ding et al. (2010) where a linear force-free field with a vertical current sheet is adopted. The initial state is assumed to be static and isothermal, with a temperature $T = T_i = 2 \times 10^4$ K representing the atmosphere in the chromosphere. The initial mass density is calculated by

$$\rho = \rho_{b0} \exp(-gy/2), \quad (4)$$

where ρ_{b0} is a free parameter used to control the mass density at the bottom.

By choosing different values of ψ_{b0} and ρ_{b0} , we can obtain four initial states represented by A1, A2, B1 and B2. The parameters of the four initial states are listed in Table 1. The initial states are divided into two groups, case A ($\psi_{b0} = 2$) and case B ($\psi_{b0} = 1$), corresponding to the initial backgrounds with strong (50 G) and weak (25 G) magnetic field strength, respectively. Then, each group is divided into two subgroups according to the value of ρ_{b0} . The case of $\rho_{b0} = 1$ ($N_e = 2 \times 10^{11}$ cm $^{-3}$) represents the initial state with high mass density, and $\rho_{b0} = 0.1$ ($N_e = 2 \times 10^{10}$ cm $^{-3}$) with low mass density. The characteristic values of Alfvén velocity (v_A) and the ratio of the gas pressure to magnetic pressure (β) corresponding to each state are also listed in Table 1. As the initial temperature of the background is the same for each state, the characteristic sound speed for all the cases are the same as well, namely 23 km s $^{-1}$.

Figure 1 (left panel) shows the configuration of the initial magnetic field for the case of A1 as an example. The initial

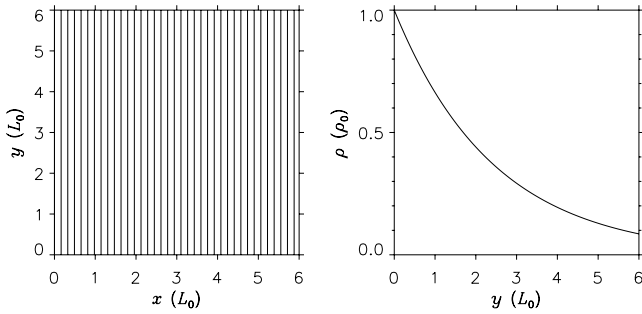


Fig. 1. Magnetic configuration of the initial potential field (*left*), and distribution of the initial mass density versus height (*right*) for case A1.

magnetic field is uniform and vertical. Figure 1 (*right panel*) shows the distribution of the initial mass density versus height for case A1. The initial mass density is also uniform along x . As the radiative loss is reduced to zero at $T = 2 \times 10^4$ K, the initial state is not only in hydrostatic equilibrium but also in thermal equilibrium.

The magnetic configuration of case A2 is the same as case A1. The distribution of the initial mass density for case A1 and A2 are similar, but its value is only one tenth of that for A2 as regards the mass density at the same height. For cases in group B, the magnetic configurations are the same. The magnetic field strength in A is twice of that in B. The distribution of the initial mass density of case B1 is the same as case A1, and that of case B2 is the same as case A2.

2.3. New magnetic flux emergence

The emergence of new magnetic flux is implemented numerically in the same way as presented in Ding et al. 2010, see Eq. (10) therein). Here, the flux emergence time is taken to be 80 s as well. The α parameter which controls the magnitude and orientation of the emerging flux is taken to be -1.2 for cases in group A, and -2.4 for cases in group B. The reason why α values are different is to keep the ratio of the newly emerging magnetic flux to the total flux of the initial background the same for case A and B, so that reconnection between the new flux and pre-existing flux occurs at a similar height in the two cases. The localized resistivity introduced to initiate magnetic reconnection is in the same form as expressed in Ding et al. (2010).

2.4. Line profiles

In order to compare the numerical simulations with observations, line profiles are calculated in terms of

$$I(\lambda, t) = \int_{x=1}^{x=4} \int_{y=y_1}^{y=y_2} \rho^2 G(T) \epsilon_T(\lambda) dx dy, \quad (5)$$

where y represents the line-of-sight, $G(T)$ is the emission contribution function, and

$$\epsilon_T(\lambda) \propto \frac{\exp - \left[\frac{(\lambda - \lambda_0 - \lambda_s)}{\Delta \lambda_0} \right]^2}{\Delta \lambda_0 \sqrt{\pi}}, \quad (6)$$

is the static line profile. In the equation above, λ_0 is the rest wavelength of the resonance line, $\lambda_s = \frac{\lambda_0}{c} v_p$ is the Doppler shift

corresponding to the line-of-sight velocity, v_p , and $\Delta \lambda_0$ is the Doppler width of the line given by

$$\Delta \lambda_0 = \frac{\lambda_0}{c} \sqrt{\frac{2k_B T}{m_i}}, \quad (7)$$

where c is the speed-of-light, k_B is the Boltzmann constant, and m_i is the ion mass. The contribution function, $G(T)$, is obtained from the ADAS database (Summers 2004), and ionization equilibrium is considered. During the calculation of line profiles, a 1500 km wide slit, located between $1 \leq x \leq 4$ (see Fig. 3), is used. When observed with spectrometers like SUMER or EIS, line profiles from different regions of the jet can be obtained, e.g. see Figs. 7 and 8 in Madjarska (2011), where the small box outlined in Fig. 7 may be moved around to produce line profiles in a different part of the jet and/or reconnection site as seen in Fig. 8. Therefore, it is important that the simulation derived observables from various parts of a jet are studied and compared with observed line profiles from the same type of regions. We, therefore, divided the simulated regions into two parts: P1 which covers the region between $y_1 = 0$ and $y_2 = 2$, i.e. over the reconnection site and its close surroundings, and P2 between $y_1 = 2$ and $y_2 = 5$, i.e. over the entire jet. The positions of P1 and P2 are also denoted in Fig. 3. Note however, that in some cases, depending on the jet temperature and density, there may be little or no difference in the simulated profiles at the different depths/locations, see A1 case later. Furthermore, if the jet was traveling directly towards the observer with no line-of-sight inclination, then deriving of the line profiles from different jet depths/locations would not be possible. However, jets are seen propagating in any directions on the solar disk, including the example outlined above, where such a comparison is possible and therefore, needs to be investigated both observationally and theoretically.

In the present study, we will focus on the jets resulting from magnetic reconnection as seen in different parts of the solar atmosphere. Line profiles formed in the lower transition region (TR) are calculated for C III 977 Å (8×10^4 K), the upper transition region as seen in O V 629 Å (2.5×10^5 K) and the lower corona as viewed in Fe IX 171 Å (8×10^5 K).

3. Numerical results

In this section, the results of magnetic reconnection triggered by newly emerging magnetic flux are presented. Two cases are considered, case A and B, where the initial background magnetic field strength is different. In each case, two sub-cases with different initial mass density are investigated.

3.1. Case A1: cool chromosphere-TR jet

In case A1 we explore an environment with plasma characteristics $\psi_{b0} = 2$ and $\rho_{b0} = 1$, i.e. $B = 50$ G and $N_e = 2 \times 10^{11}$ cm $^{-3}$, which corresponds to high field strength typical of an active region and high density environment. Figure 2a shows the evolution of the magnetic field, temperature, and velocity for this case. As the new magnetic flux with negative polarity ($\alpha < 0$) emerges, the background magnetic field lines will be pushed out towards $x = 0$, resulting in horizontal flows. A current sheet is then formed at the right-hand side of the newly emerging magnetic arcade. If magnetic diffusion is introduced into the current sheet, magnetic reconnection will occur. Part of the magnetic field lines expand outward (towards the upper-left in Fig. 2), and the plasma at the right-hand side of the flux emergence region

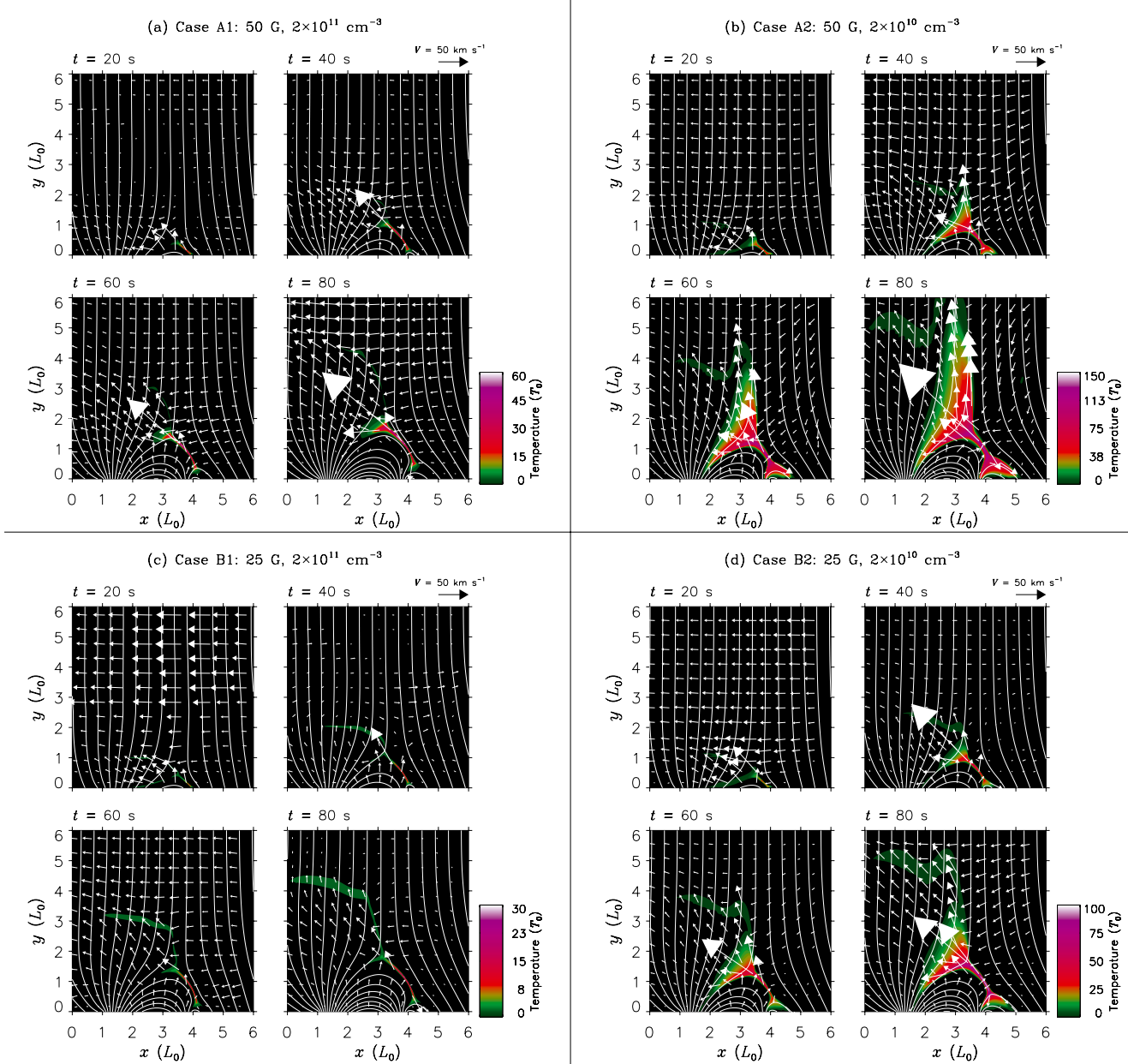


Fig. 2. Evolution of the magnetic field (solid lines), temperature (colour), and velocity (arrows) at four times for case A1 **a**), A2 **b**), B1 **c**) and B2 **d**). The characteristic parameters of magnetic field strength and electron number density are given above each case plot. Note that the colour-coding is different for each run.

is pushed into the diffusion region. As reconnection goes on, the expansion of magnetic field lines propagates to higher regions, where plasma is dragged by the magnetic field and moves towards the left as seen in the figure. At the same time, magnetic field lines together with plasma from the right-hand boundary are driven leftwards due to pressure imbalance. This causes strong horizontal flows at higher altitude, as seen at $t = 60$ s and 80 s in Fig. 2a. These horizontal flows will collide with the upward outflows as a result of magnetic reconnection, and a shock is formed at the interface. In order to show the shock, the state at $t = 80$ s in Fig. 2a is re-plotted in Fig. 3 where the temperature is plotted using a smaller colour scale. At the interface of the horizontal flows and upward outflows, a bundle of plasma hotter than its surrounding is clearly seen. During the magnetic reconnection, the plasma in the diffusion region is heated by Joule dissipation. The outflows, as a result of magnetic

reconnection is bi-directional, upward and downward, along the current concentration. In our model, only part of the down-flow is visible because of the low X-point.

Figure 4 (*top left*) shows the maximum jet velocity (*solid line*) and its line-of-sight component (*dotted line*) measured at P1, as a function of time. The corresponding plasma temperature at the location of the maximum jet velocity is also shown in Fig. 4 (*bottom left*), as a function of time. During the process of magnetic reconnection, the jet is accelerated by magnetic tension forces, reaching a velocity of 150 km s^{-1} at $t = 80$ s in the P1 region, with a line-of-sight velocity of 100 km s^{-1} . The temperature of the jets with peak velocity is about $4 \times 10^5 \text{ K}$ ($20 T_i$) at maximum. These measurements would correspond to a region at the foot-points of a chromospheric jet. The same physical quantities are also measured at P2, where the jet velocity only reaches 45 km s^{-1} at maximum and the jet temperature

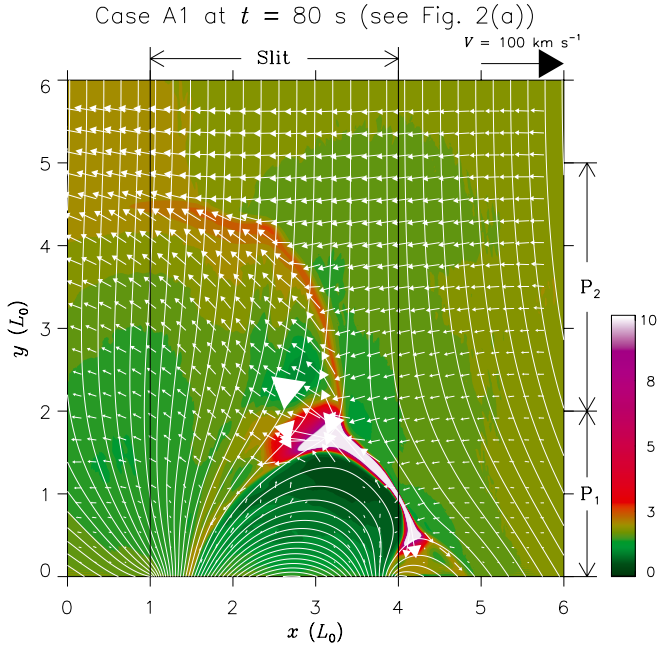


Fig. 3. Re-plot of the state at $t = 80$ s in Fig. 2a. The temperature is shown in a smaller color scale than in Fig. 2a. The two solid lines (black) denote the x -position of the slit, and P1 and P2 denote the two y -position of the slit.

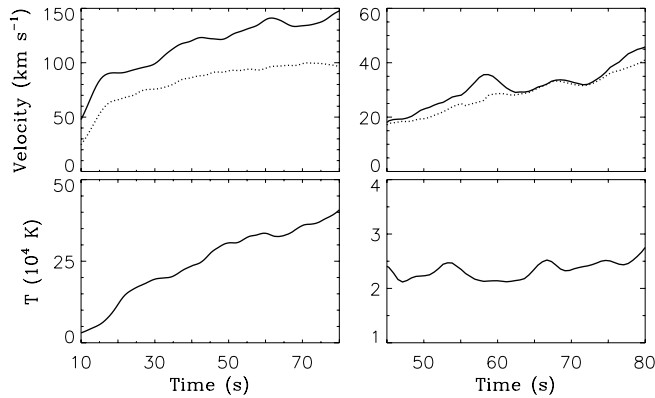


Fig. 4. Evolution of the physical quantities, e.g. maximum jet velocity (solid line, top row), its line-of-sight component (dotted line, top row), and plasma temperature (bottom row) at the location of the peak jet velocity, for case A1. Left column: measured at P1; right column: measured at P2.

is $\approx 2\text{--}3 \times 10^4$ K ($1\text{--}1.5 T_i$). These plasma parameters describe a short jet reaching only typical chromospheric temperatures propagating at a speed which is comparable with observed values of fibrils.

Figure 5 (top row) shows the C III 977 Å line (top left), O v 629 Å line (top middle), and Fe ix 171 Å line profiles (top right) measured at P1 at four times, $t = 20, 40, 60, 80$ s. The line profiles are plotted as a function of the Doppler velocity (v_p), instead of wavelength (λ), in terms of the expression $v_p = c\lambda_s/\lambda_0$. In our line profile calculations the jets propagate towards the observer, i.e. the observer is at the top of the y -axis. Therefore, blue-shifted emission corresponds to plasma moving from the bottom to the top of the y -axis ("+"), while red-shifted emission is associated with plasma moving in the opposite direction ("−"), i.e. away from the observer. Whereas in the defi-

nition of Doppler velocities, blue-shifts are regarded as negative values and red-shifts as positive. Therefore, the velocity values obtained in our simulations need to be reversed in the calculations of line profiles, so as to get the same expression of Doppler velocities as in the observations. It is shown that the maximum blue-shifts reach 60 km s^{-1} at $t = 80$ s for the C III 977 Å line, and $\sim 90 \text{ km s}^{-1}$ for both O v 629 Å and Fe ix 171 Å. All the line profiles show at least a two-Gaussian structure.

For C III 977 Å, the radiance of the red-shifted component increases during the interval $t = 20$ s to 40 s, and then decreases. The red-shifted component centers around velocity 0, which is mainly contributed by the plasma in and/or close to the diffusion region. From $t = 20$ s to 40 s, more plasma is heated, but to a temperature less than 2×10^5 K (which is the upper threshold of the contribution function for C III 977 Å). As the plasma is heated to above this temperature, its contribution to C III line becomes very weak and negligible. The blue-shifted component comes from the plasma outside the diffusion region. It is closer to the diffusion region at $t = 20$ s, and has a strong emission. Later, the hot region expands, but the high velocity region expands slowly and its mass density becomes low, leading to a decrease in the blue-shifted component at $t = 40$ s. As more plasma is heated and accelerated, blue-shifted emission starts to increase from $t = 40$ s to 60 s. For O v 629 Å, the radiance of the highly blue-shifted components increases from $t = 20$ s to 40 s. This is because more plasma is heated to higher transition-region temperatures. As the temperature increases to above 2.5×10^5 K (i.e. the temperature of maximum ionization (T_{\max}) for O v 629 Å) after $t = 40$ s, the contribution of the hot plasma to the O v 629 Å line becomes weaker. Then, the radiance of the highly blue-shifted components decreases, which corresponds to the increase of the radiance of the blue-shifted components for Fe ix 171 Å line.

Figure 6 shows the line profiles of C III 977 Å line measured at P2, where the blue-shift is 20 km s^{-1} at $t = 60$ s and reaches $\sim 30 \text{ km s}^{-1}$ at $t = 80$ s. There is no C III emission at $t = 20$ and 40 s, because the up-flow jets reach P2 region after $t = 40$ s. In addition, when measured at P2, the O v 629 Å line and Fe ix 171 Å have no detectable emission.

The results in case A1 are summarized in Table 2, where the maximum velocity of the jet (V_{jet}), its line-of-sight component (V_y), the plasma temperature (T_{jet}) at the position of the maximum jet velocity, and blue shifts for C III 977 Å (V_C), O v 629 Å (V_O), and Fe ix 171 Å line (V_{Fe}) are calculated at two positions, P1 and P2, respectively. All the values shown in the table are the maximum ones obtained in 80 s. The results for other cases, namely A2, B1 and B2, which are discussed in detail in the following sections, are also listed similarly in Table 2.

For the A1 case, line profiles are also calculated over the whole height, e.g. $y = 0\text{--}6$, as shown in the bottom row in Fig. 5. There is very small difference of line profiles at P1 and that of the whole height. In fact, the line profiles at two different depths are the same for O v 629 Å line and Fe ix 171 Å lines, respectively, this is because there is a zero contribution in the O v and Fe ix emission above the P1 region.

3.2. Case A2: hot transition region jet

In the A2 case, the magnetic field background is of the same strength as in case A1, i.e. 50 G, but the environment has a lower electron density ($N_e = 2 \times 10^{10} \text{ cm}^{-3}$), i.e. typical of a region formed higher in the atmosphere than the A1 case. Figure 2b shows the evolution of the magnetic field, temperature, and the

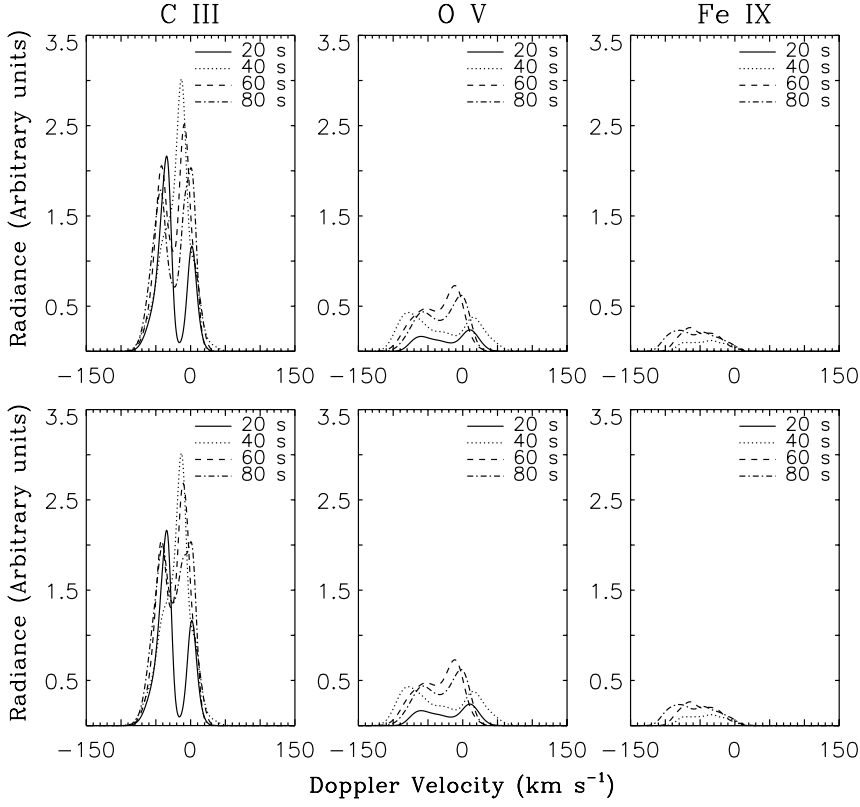


Fig. 5. Line profiles for the C III 977 Å line (left column), the O v 629 Å line (middle column), and the Fe ix 171 Å line (right column) at four times for case A1. Calculations are performed at two positions: P1 (top row) and over the whole region ($y = 0-6$, bottom row).

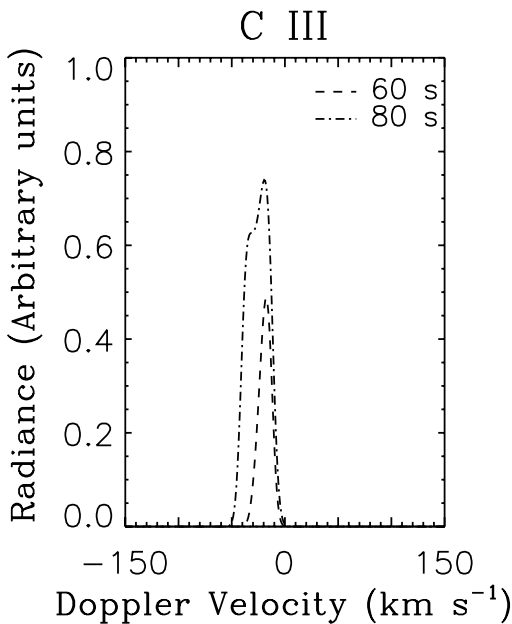


Fig. 6. Line profiles calculated at P2 for C m 977 Å line at two times for case A1. The radiance is shown as a function of the Doppler shift.

velocity. The plasma in the diffusion region is heated to higher temperatures, about 1.5×10^6 K ($75 T_i$) at maximum, compared with the case of A1. Because an environment with lower density is considered, hotter plasma (i.e. transition-region temperature and above) spreads over a larger region (this corresponds to about 700 km wide and 3000 km high) at $t = 80$ s, whereas the

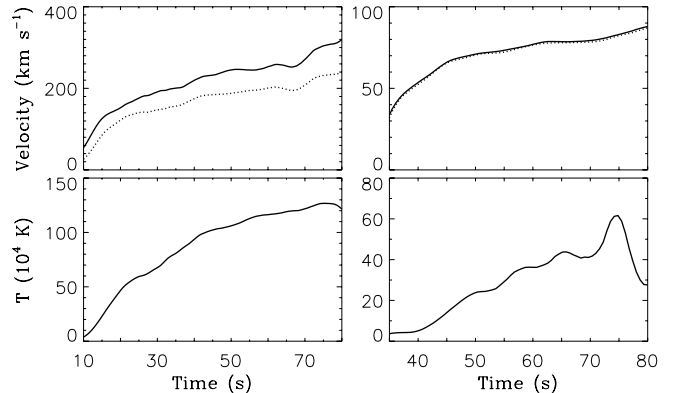


Fig. 7. Evolution of the physical quantities, e.g. maximum jet velocity (solid line, top row), its line-of-sight component (dotted line, top row), and the plasma temperature (bottom row) at the location of the peak jet velocity for case A2. Left column: measured at P1, and right column: measured at P2.

hotter plasma region is only ~ 100 km wide and ~ 1000 km high in the A1 fibril case. The decrease in density will increase the ratio of Joule heating to radiative losses, so that the plasma in the diffusion is more strongly heated. Moreover, the hot plasma is ejected outward, which will also heat the plasma outside the diffusion region. As the background atmosphere is at lower density, the energy losses of the heated hot plasma outside the diffusion region by radiation becomes small, so that the plasma over a larger area remains hot.

Figure 7 shows the maximum jet velocity (solid line, top row), its line-of-sight component (dotted line, top row), and the plasma temperature at the peak jet velocity (bottom row) as a function of time, for the A2 case. At P1 (left column), the up-flow

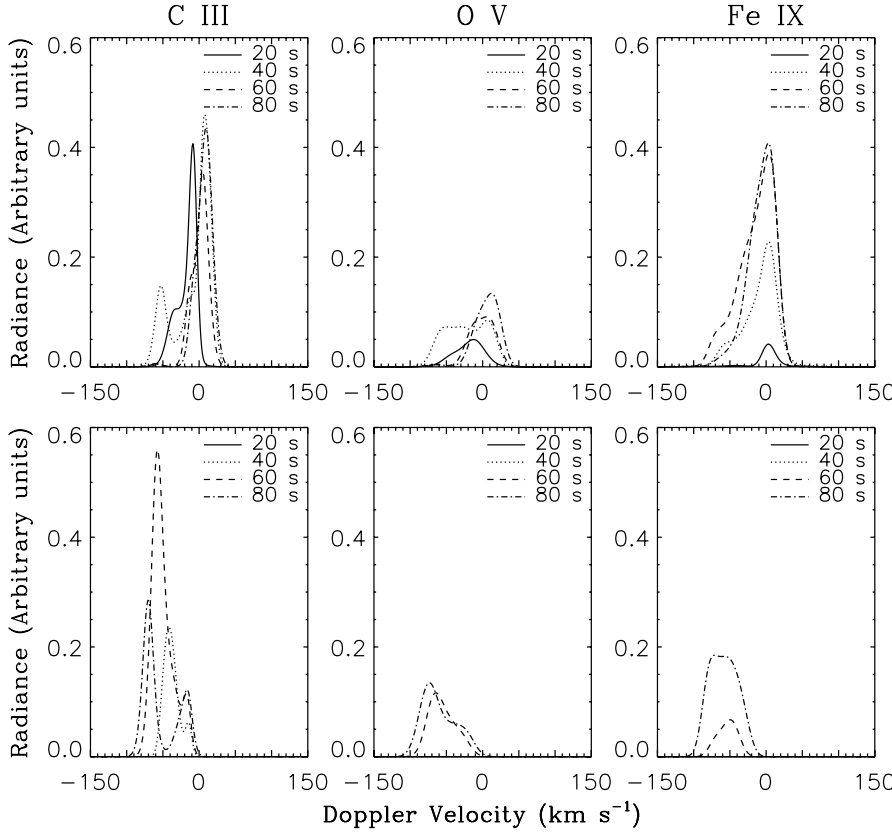


Fig. 8. Line profiles of C III 977 Å line (left column), O V 629 Å line (middle column), and Fe IX 171 Å line (right column) at four times for case A2, where the line radiance is shown as a function of Doppler shift. Each row shows the observations between certain heights. Top row: $y_1 = 0$ and $y_2 = 2$ (P1); bottom row: $y_1 = 2$ and $y_2 = 5$ (P2).

Table 2. Summary of the results for all the cases, namely case A1, A2, B1, and B2, where “—” means no signal.

	Quantity	A1	A2	B1	B2
At P1	V_{jet} (km s ⁻¹)	150	320	97	180
	V_y (km s ⁻¹)	100	240	60	130
	T_{jet} (T_i)	20	65	3.5	35
	V_C (km s ⁻¹)	60	70	70	50
	V_O (km s ⁻¹)	90	70	—	50
	V_{Fe} (km s ⁻¹)	90	70	—	50
At P2	V_{jet} (km s ⁻¹)	45	90	38	64
	V_y (km s ⁻¹)	40	90	32	63
	T_{jet} (T_i)	~1–1.5	30	~1–1.5	11
	V_C (km s ⁻¹)	30	80	35	50
	V_O (km s ⁻¹)	—	90	—	50
	V_{Fe} (km s ⁻¹)	—	90	—	—

Notes. See text for details.

jets reach 320 km s⁻¹ at maximum, line-of-sight component being 240 km s⁻¹. The temperatures of the up-flow jets with maximum velocity reach about 1.3×10^6 K ($65 T_i$). It seems that the outflow jets with high velocity and high temperature are comparable to hot X-ray jets. When observed at P2 (right column), however, both the velocities and temperatures are smaller: the jet velocity and its line-of-sight component reach about 90 km s⁻¹ at maximum, its temperature being about 6×10^5 K ($30 T_i$) at maximum. This means that a jet at transition region temperatures is produced. The differences between the jet velocity and its line-of-sight component are very small, showing that the outflows with maximum velocity are almost vertical. Moreover, there is a sharp drop in the temperature of the up-flow jets with peak

velocity between $t = 75$ and 80 s. This is because the outflows reach maximum velocity at higher altitudes, where the plasma temperature is low.

Figure 8 shows the line profiles of the C III 977 Å line (left column), the O V 629 Å line (middle column), and the Fe IX 171 Å line (right column) at four times, $t = 20, 40, 60, 80$ s, as a function of Doppler velocity. Line profiles are calculated at two positions: P1 (top row) and P2 (bottom row). Observed at P1, the maximum blue-shifts are of the order of 70 km s⁻¹ for all three lines. The intensity of C III 977 Å and O V 629 Å is a factor of 2–3 lower than in the A1 fibril case, while Fe IX 171 Å is larger. The blue-shifted components of all three lines are stronger when observed at P2 than at P1 at $t = 80$ s, whereas the red-shifted components are absent at P2. In this case of TR temperatures and relatively strong magnetic field, the produced jet is capable of reaching high TR temperatures which can peak for a short period of time at low coronal temperatures. Depending on the line-of-sight, the observer may see a mixture of P1 and P2, and in instances where the jet is moving directly towards the observer, we will see the sum of P1 and P2 line profile.

From an observational point of view, we should expect a small-scale brightening to occur at coronal temperatures but a jet will only be detected at transition region temperatures. This type of phenomena are already seen in multi-instrument observations and described by Subramanian et al. (2011). The line profiles composed of multi-component blue-shift and a redshift in transition region lines are similar to observable line profiles which describe the so-called “explosive events” (EEs). Note, however, that EE spectral line profiles were also associated with a surge in the plage area of active region (Madjarska et al. 2009) as well as were linked to EUV jets (Madjarska et al., in prep.).

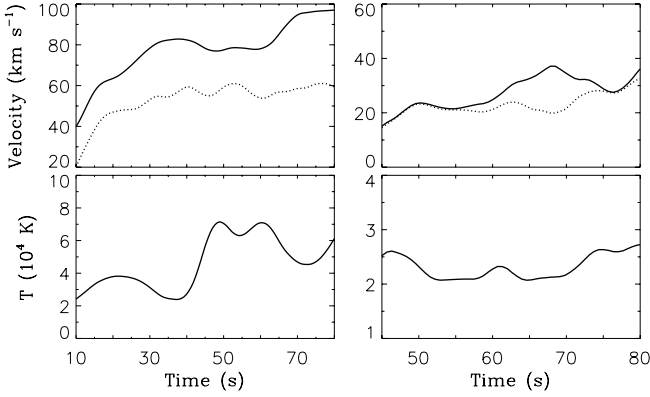


Fig. 9. Evolution of the physical quantities, e.g. maximum up-flow jet velocity (*solid line*, top row), its line-of-sight component (*dotted line*, top row), and the plasma temperature (*bottom row*) at the location of the peak jet velocity for case B1. *Left column*: measured at P1; *right column*: measured at P2.

3.3. Case B1: cool chromospheric jet

Here, the physical environment has a weaker magnetic field strength of 25 G, and a high plasma density ($N_e = 2 \times 10^{11} \text{ cm}^{-3}$). Figure 2c shows the evolution of the magnetic field, temperature, and velocity. The physical process is the same as explained in Sect. 3.1, i.e. horizontal flows and a shock interface between the inflows and outflows. The plasma in the diffusion region is heated to $3 \times 10^5 \text{ K}$ ($15 T_i$). The scale of the hot plasma region (i.e. transition-region temperature) is very small, 50 km in width and 800 km in height, i.e. a sub-arcsec region.

In Fig. 9 at P1, the velocity of the up-flows (*solid line*, top left) reaches $\sim 100 \text{ km s}^{-1}$ at maximum, with a line-of-sight component (*dotted line*, top left) of $\sim 60 \text{ km s}^{-1}$. The temperature of the up-flows with maximum velocity is $\sim 6 \times 10^4 \text{ K}$ ($3 T_i$). At P2 (right column in Fig. 9), the maximum jet velocity (*solid line*, top right) is only $\sim 40 \text{ km s}^{-1}$ at maximum, and the jet temperature (*bottom right*) is $2-3 \times 10^4 \text{ K}$ ($1-1.5 T_i$). Therefore, a cold jet that propagate with relatively low speed is produced as compared to cases A1 and A2.

Figure 10 shows the line profiles for C III 977 Å at four times. At P1 (left) the blue-shifts reach about $60-70 \text{ km s}^{-1}$ at maximum, while at P2 (right), the blue-shifts are only about $25-35 \text{ km s}^{-1}$. As the hotter plasma region is small in scale, the emission at higher altitude is weak or absent. The temperatures is not high enough to produce sufficient O v 629 Å and Fe ix 171 Å line emission. A small-scale brightening associated with the diffusion region should be detected in transition region lines, while a small-scale jet could only be seen at low transition region temperatures at maximum.

3.4. Case B2: cool chromosphere-TR jet

The results of case B2 are also analyzed similarly, see Figs. 2d, 11, 12, and 13. In this case, we have a lower electron density, $N_e = 2 \times 10^{10} \text{ cm}^{-3}$, and a field strength as in B1, i.e. 25 G. It shows that the plasma in the diffusion region is heated up-to 1 MK ($50 T_i$) at maximum. Observed at P1 (left column in Fig. 11), the maximum velocity of the up-flows reaches 180 km s^{-1} at maximum, with 130 km s^{-1} in the line-of-sight component. The temperature of the up-flow jets with maximum velocity reaches $7 \times 10^5 \text{ K}$ ($35 T_i$). At P2 (right column in Fig. 11), both the maximum jet velocity and its line-of-sight

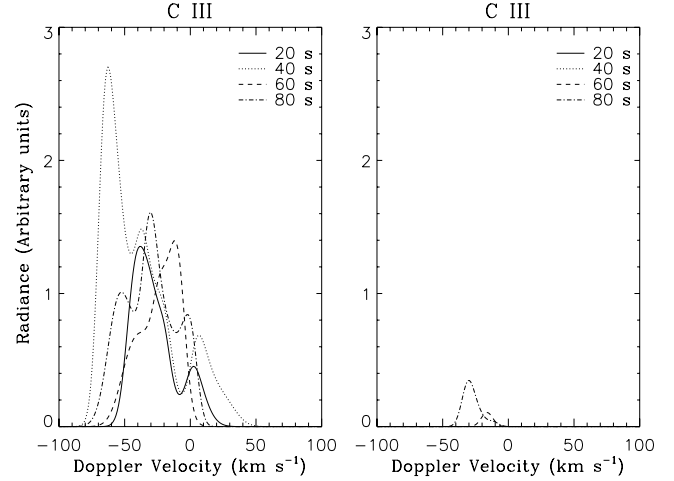


Fig. 10. Line profiles of C III 977 Å line observed at P1 (left) and P2 (right) at four times for the case of B1, where the line radiance is shown as a function of Doppler shift.

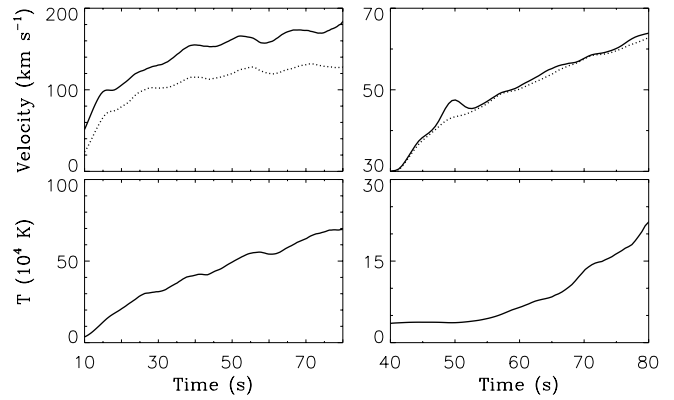


Fig. 11. Evolution of the physical quantities, e.g. maximum up-flow jet velocity (*solid line*, top row), its line-of-sight component (*dotted line*, top row), and the plasma temperature (*bottom row*) at the location of the peak jet velocity for case B2. *Left column*: measured at P1; *right column*: measured at P2.

component are $\sim 60 \text{ km s}^{-1}$ at maximum. Moreover, after $t = 60 \text{ s}$, the temperature of the up-flow jets with maximum velocity increases. This is because the outflows get maximum velocity at low altitude, where the plasma is heated to higher temperature. In this environment, the line profiles of all three lines show a Doppler shift of 50 km s^{-1} , when calculated at P1 (Fig. 12). At P2 (Fig. 13), both C III 977 Å line and O v 629 Å line show blue-shifts of 50 km s^{-1} as well. The emission in the Fe ix 171 Å line is absent, however, when observed at P2. We should be able to register observationally an event which starts with a brightening at coronal temperatures, but jets will only be seen at transition region temperatures.

4. Conclusions and discussions

Numerical studies on magnetic reconnection caused by new magnetic flux emergence, occurring at densities typical of the chromosphere and transition region, starting in an environment with a temperature of $2 \times 10^4 \text{ K}$ (T_i) are presented. The magnetic field strength is set at 25 G and 50 G, which are the typical observed values for chromospheric jets like spicules (quiet Sun)

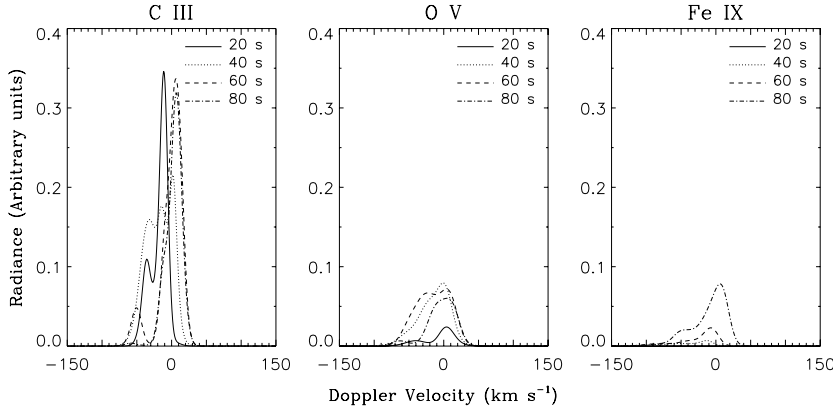


Fig. 12. Line profiles of C III 977 Å line (left), O V 629 Å line (middle), and Fe IX 171 Å line (right) at four times for case B2 at P1, where the line radiance is shown as a function of Doppler shift.

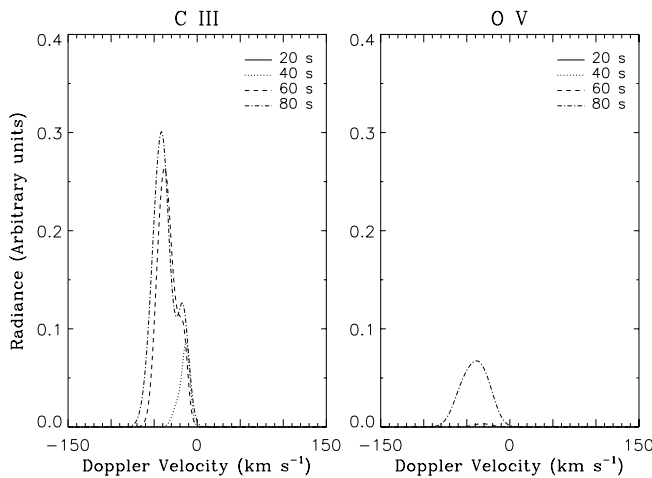


Fig. 13. Line profiles of C III 977 Å line (left) and O V 629 Å line (right) at four times for case B2 at P2, where the line radiance is shown as a function of Doppler shift.

and fibrils (active region). It is shown that the results are strongly dependent on the physical environment: a decrease of one order of magnitude of the density leads to a one time increase of the maximum jet velocity; an increase of two times the magnitude of the magnetic field strength leads to the same velocity enhancement. Here, the ratio of the amount of the newly emerging magnetic flux to that of the initial background is kept the same in all cases considered. If less new flux is emerged, or the flux emergence time is longer, the maximum velocity and temperature of the outflow jets will be weaker. Furthermore, both the inclination and non-uniformity of the initial background magnetic field will have an effect on the velocity and temperature of the outflow. Line profiles of two transition region lines (C III 977 Å and O V 629 Å), plus the lower coronal line (Fe IX 171 Å) are calculated at two positions: a region which covers the reconnection site and its close surroundings, and a region which covers the entire jet for all four cases. The simulated response in these spectral line is an important observable which can directly be compared with observed line profiles in various types of jets.

In the case where we have a lower electron density ($N_e = 2 \times 10^{10} \text{ cm}^{-3}$), i.e. more typical for the transition region, and a stronger magnetic field of 50 G, up-flows with line-of-sight velocities as high as 200 km s⁻¹ and temperatures around 1 MK ($50 T_i$) can be produced around the reconnection site. The jet

at P2, however, reaches ~90 km s⁻¹, but its temperatures is only $6 \times 10^5 \text{ K}$ ($30 T_i$) at maximum, i.e. upper transition region temperatures. As a result, Fe IX 171 Å has weak or no detectable emission. The opposite case of high density plasma ($N_e = 2 \times 10^{11} \text{ cm}^{-3}$), typical for the chromosphere and weaker magnetic field of 25 G, results in a jet with a velocity of ~40 km s⁻¹ and a temperature $\sim 2-3 \times 10^4 \text{ K}$ ($1-1.5 T_i$), respectively. Therefore, a weak magnetic field in a high-density plasma results in a jet not higher than the typical chromospheric values.

Karpen et al. (1995) studied chromospheric eruptions caused by shear-induced magnetic reconnection. This work used a much larger box with the shear reaching the X-point after 300 s and concluded that the dynamics of chromospheric eruptions were dependent on the geometry, shear strength, and local resistivity. The present study is an important attempt to test the formation of jets originating in the lower solar atmosphere as produced only by magnetic reconnection triggered by new flux emergence. Here, we do not look into the emergence rate, the emergence time or the amount of the newly emerging magnetic flux which are important factors that could effect the results of the jets. Instead, we study the effect of changing the field strength and electron density. The parameters have a significant influence on the temperature and velocity of the outflow jets. The results demonstrate that magnetic reconnection could be an efficient mechanism to drive plasma outflows in the chromosphere and transition region. It is shown that if the magnetic field is below 50 G, the jets can be accelerated to relatively high velocities, but their temperatures remain in the typical chromosphere – transition region range. This work suggests that intensive studies on small-scale jets and the magnetic fields associated with them together with a detailed spectroscopic evaluation of the jet plasma parameters are needed in order to confirm or reject the driving mechanism tested here and permit an evaluation of their contribution to the mass and energy balance in the solar atmosphere.

Yokoyama & Shibata (1995, 1996) performed simulations of magnetic reconnection based on a 2D magnetic flux emergence model. A huge amount of new magnetic flux is emerged and evolves to the coronal heights where the reconnection with the pre-existing background magnetic flux actually occurs. The magnetic field strength and mass density around the diffusion region are similar to what we use in case B1 where jets with low temperature and low velocity are obtained in our study. In the Yokoyama & Shibata study, with the reconnection occurring in the corona (note that both heat conduction and radiative effects were neglected in their study), hot X-ray jets were produced.

Furthermore, the emergence of new flux also carried cold and dense plasma upward, which will then be accelerated by magnetic tension, generating cool jets.

Nishizuka et al. (2008) explored MHD simulations of new flux emergence, triggering magnetic reconnection by adopting similar initial conditions to Yokoyama & Shibata (1995, 1996), but with a hotter (1 MK) and less dense (10^{10} cm^{-3}) corona. Hot X-ray jets (as high as 10 MK), i.e. hotter than in Yokoyama & Shibata (1995, 1996), were obtained.

Murray et al. (2009) studied oscillatory reconnection by inserting a magnetic flux tube below the solar surface. In their experiment the background initial magnetic field is $\sim 20 \text{ G}$, and the initial density decreases from $\sim 10^{17} \text{ cm}^{-3}$ in the lower photosphere to $\sim 10^9 \text{ cm}^{-3}$ in the upper corona. The evolution time of the magnetic reconnection is very long ($\sim 50 \text{ min}$) for the reconnection system to get close to an equilibrium state around which reconnection reversals occur. Once the system reaches an equilibrium, the reconnection ceases. The velocity of the jets shown in their paper are slow ($\sim 50 \text{ km s}^{-1}$). However, as the reconnection occurs in the corona, the temperature of the jets is high, reaching a few MK. Heat conduction and radiative losses were neglected in their simulations as well.

In the present study the solar atmosphere is fully ionized. In the solar corona this approximation is reasonable. However, in the lower solar atmosphere, e.g. photosphere and chromosphere, the plasma is partially ionised, which means neutrals are omnipresent. Due to the collisions with neutrals, in particular ion-neutral collisions, a Cowling resistivity is introduced into the Ohm's law (Khodachenko et al. 2004; Arber et al. 2007; Soler et al. 2009, and references therein). As a result, the Joule heating is changed to $Q_{\text{Joule}} = \eta j_{\parallel}^2 + \eta_c j_{\perp}^2$, where η , η_c , j_{\parallel} , j_{\perp} are the Coulomb and Cowling resistivity, and the components of the current density parallel and perpendicular to the magnetic field, respectively. As far as a 2D MHD model is concerned, the electric currents are perpendicular to the magnetic field, and thus, the Joule heating term is simplified to $Q_{\text{Joule}} = \eta_c j_{\perp}^2 = \eta_c j^2$. In the chromosphere, $\eta_c/\eta \gg 1$ (Khodachenko et al. 2004; Leake & Arber 2006), which means that the resistivity is increased when a partially ionized plasma is considered which will result in a lower magnetic Reynolds number. Litvinenko & Chae (2009) suggests the use of an enhanced value of effective resistivity, instead of the classical resistivity (η), in studying magnetic reconnection in the chromosphere.

In the calculations of line profiles, ionization equilibrium means the contribution function is mainly dependent on the electron temperature but weakly on the electron number density. This is reasonable for the cases where the velocity of the outflow is small, e.g. see Peter et al. (2004). Peter et al. (2006) found that the assumption of ionization equilibrium is acceptable for cases with higher velocity if the temperature gradient is small. In our simulations, strong jets are obtained in some environments, e.g. case A2. Despite this, the scale of such strong jets with velocities greater than 100 km s^{-1} is very small, mainly around the diffusion region. Over a much larger scale, the velocities of the outflow jet is small, see top left panel (measured at P2) in Fig. 4. Furthermore, there is a sharp density increase between the hot up-flow jet and the cold background plasma, which is helpful for the reduction of ionization and recombination times. Inside

the hot up-flow region, the temperature gradient is much flatter and in order to calculate the line emission more precisely, it may be necessary to take into account the time-dependent ionization in further studies, e.g. see work by Sarro et al. (1999); Roussev et al. (2001b).

Acknowledgements. Research at Armagh Observatory is grant-aided by the N. Ireland Dept. of Culture, Arts and Leisure (DCAL). This work was supported via a grant (ST/F001843/1) from the UK Science and Technology Facilities Council. M.M. and J.G.D. thank the International Space Science Institute, Bern for the support of the team "Small-scale transient phenomena and their contribution to coronal heating".

References

- Arber, T. D., Haynes, M., & Leake, J. E. 2007, ApJ, 666, 541
 Beckers, J. M. 1968, Sol. Phys., 3, 367
 Cook, J. W., Brueckner, G. E., Bartoe, J., & Socker, D. G. 1984, Adv. Space Res., 4, 59
 Cook, J. W., Cheng, C., Jacobs, V. L., & Antiochos, S. K. 1989, ApJ, 338, 1176
 De Pontieu, B., Hansteen, V. H., Rouppe van der Voort, L., van Noort, M., & Carlsson, M. 2007, ApJ, 655, 624
 Dere, K. P., Bartoe, J., Brueckner, G. E., Cook, J. W., & Socker, D. G. 1989, Sol. Phys., 119, 55
 Ding, J. Y., Madjarska, M. S., Doyle, J. G., & Lu, Q. M. 2010, A&A, 510, A111
 Galsgaard, K., Moreno-Insertis, F., Archontis, V., & Hood, A. 2005, ApJ, 618, L153
 Hansteen, V. H., De Pontieu, B., Rouppe van der Voort, L., van Noort, M., & Carlsson, M. 2006, ApJ, 647, L73
 Heggland, L., De Pontieu, B., & Hansteen, V. H. 2007, ApJ, 666, 1277
 Heggland, L., De Pontieu, B., & Hansteen, V. H. 2009, ApJ, 702, 1
 Hu, Y. Q. 1989, J. Comput. Phys., 84, 441
 Innes, D. E., & Tóth, G. 1999, Sol. Phys., 185, 127
 Jiang, R. L., Shibata, K., Isobe, H., & Fang, C. 2011, ApJ, 726, L16
 Jin, S., Inhester, B., & Innes, D. 1996, Sol. Phys., 168, 279
 Karpen, J. T., Antiochos, S. K., & DeVore, C. R. 1995, ApJ, 450, 422
 Khodachenko, M. L., Arber, T. D., Rucker, H. O., & Hanslmeier, A. 2004, A&A, 422, 1073
 Leake, J. E., & Arber, T. D. 2006, A&A, 450, 805
 Litvinenko, Y. E., & Chae, J. 2009, A&A, 495, 953
 Madjarska, M. S. 2011, A&A, 526, A19
 Madjarska, M. S., Doyle, J. G., & de Pontieu, B. 2009, ApJ, 701, 253
 Madjarska, M. S., Vanninathan, K., & Doyle, J. G. 2011a, A&A, 532, L1
 Martínez-Sykora, J., Hansteen, V., & Moreno-Insertis, F. 2011b, ApJ, 736, 9
 McClymont, A. N., & Canfield, R. C. 1983, ApJ, 265, 497
 Murray, M. J., van Driel-Gesztelyi, L., & Baker, D. 2009, A&A, 494, 329
 Nishizuka, N., Shimizu, M., Nakamura, T., et al. 2008, ApJ, 683, L83
 Pariat, E., Antiochos, S. K., & DeVore, C. R. 2009, ApJ, 691, 61
 Pariat, E., Antiochos, S. K., & DeVore, C. R. 2010, ApJ, 714, 1762
 Patsourakos, S., Pariat, E., Vourlidas, A., Antiochos, S. K., & Wuelser, J. P. 2008, ApJ, 680, L73
 Peter, H., Gudiksen, B. V., & Nordlund, Å. 2004, ApJ, 617, L85
 Peter, H., Gudiksen, B. V., & Nordlund, Å. 2006, ApJ, 638, 1086
 Rosdahl, K. J., & Galsgaard, K. 2010, A&A, 511, A73
 Roussev, I., Doyle, J. G., Galsgaard, K., & Erdélyi, R. 2001a, A&A, 380, 719
 Roussev, I., Galsgaard, K., Erdélyi, R., & Doyle, J. G. 2001b, A&A, 370, 298
 Roussev, I., Galsgaard, K., Erdélyi, R., & Doyle, J. G. 2001c, A&A, 375, 228
 Sarro, L. M., Erdélyi, R., Doyle, J. G., & Pérez, M. E. 1999, A&A, 351, 721
 Soler, R., Oliver, R., & Ballester, J. L. 2009, ApJ, 699, 1553
 Sterling, A. C., Shibata, K., & Mariska, J. T. 1993, ApJ, 407, 778
 Subramanian, S., Madjarska, M. S., Doyle, J. G., & Bewsher, D. 2011, A&A, in press
 Summers, H. P. 2004, The ADAS User Manual, version 2.6,
<http://www.adas.ac.uk/manual.php>
 Tavabi, E., Koutchmy, S., & Ajabshirizadeh, A. 2011, New A, 16, 296
 Tsiroupolia, G., & Schmieder, B. 1997, A&A, 324, 1183
 Withbroe, G. L. 1983, ApJ, 267, 825
 Yokoyama, T., & Shibata, K. 1995, Nature, 375, 42
 Yokoyama, T., & Shibata, K. 1996, PASJ, 48, 353